npj | climate and atmospheric science

Article

Published in partnership with CECCR at King Abdulaziz University

https://doi.org/10.1038/s41612-024-00884-y

# Novel perspectives on multiple-peak diurnal convection over a tropical mountainous island from idealized large-eddy simulations



Yu-Hsiu Wang, Wei-Ting Chen ✉ & Chien-Ming Wu

Two robust peaks in the diurnal evolution of orographically-locked precipitation are simulated in large-eddy simulations with an idealized ocean-plain-mountain topography. The ensemble experiment design is guided by sounding statistics from summertime afternoon thunderstorms in Taiwan to obtain realistic variability of free-tropospheric moisture associated with the intensity of the summertime subtropical high. The convection in the first peak is directly modulated by convective available potential energy, while the convection in the second peak is associated with low-level moist static energy (MSE) transport by the island-scale (40-km) local circulation, producing more extreme rainfall. When the initial free troposphere is drier, the convection in the second peak is strengthened. Both the environmental adjustments by the first peak and local circulation development contribute to the sensitivity of the second peak to free-tropospheric moisture. This work highlights the critical roles of convection-environment interaction and upstream MSE supply in enhancing extreme diurnal precipitation over complex topography.

Diurnal convection plays a critical role in the global climate system as it drives circulation and significantly influences the energy balance and hydrological cycle[1,2] by redistributing heat[3,4] and moisture[5] within the atmosphere. Previous research has revealed patterns of active diurnal convective systems and precipitation over tropical islands, such as the Maritime Continent (MC) region. Over these islands, convective activity tends to peak in the late afternoon and evening over islands[6,7] and propagate inland[8,9]. The development of diurnal convection is modulated by the intricate interactions among radiation[10–12], diurnal land-sea circulation[13–15], and organized convective systems[16].

Previous studies reveal that the characteristics of tropical diurnal convection, including the peak intensity and timing, can respond to the large-scale environment associated with synoptic, intraseasonal, and interannual variability (e.g.[17–21]). When examining the temporal evolution of diurnal rainfall, many studies adopted a simplified depiction of a smooth cycle with a single peak. Curve fitting or frequency filtering is often applied to the time series to extract the leading harmonics and, thereby, obtaining the peak time and amplitude as the first-order characteristics of the diurnal cycle over a specific location. However, observations with hourly (or more frequent) sampling can reveal the existence of multiple peaks in the temporal evolution from noon to evening, such as those observed in the GoAmazon campaign[22]. As the long-term rain gauge network observations in Taiwan provides the valuable observational record to study diurnal precipitation over complex terrain, the statistics over the southwestern regions of the island also confirm that multiple precipitation peaks can sometimes occur within the diurnal evolution (Fig. 1a), and there is a higher probability to detect the multiple-peak feature over the mountainous sites (Fig. 1b). These observed details showcase the complexity in the diurnal convection evolution. We hypothesize that the multiple peaks are caused by distinct physical processes rather than by statistical variations due to changing environmental conditions. The development of moisture in the atmosphere is considered an important factor contributing to the variabilities in diurnal convection. Previous studies point out that, generally in a moister environment, diurnal convection tends to initiate earlier[22,23] and exhibit higher intensity[24]. This is attributed to less entrainment in convection, which promotes more significant convection development[25] and the release of more instability[22]. In the scenario of multiple convective peaks, the sensitivity to ambient conditions may be modulated if the earlier convection provides the pre-conditions of the later convection. Therefore, the underlying physical processes regarding the formation of different precipitation peaks, as well as their response to environmental conditions, are worth of dedicated investigation in order to appropriately understand how the

Department of Atmospheric Sciences, National Taiwan University, Taipei, Taiwan. ✉e-mail: weitingc@ntu.edu.tw

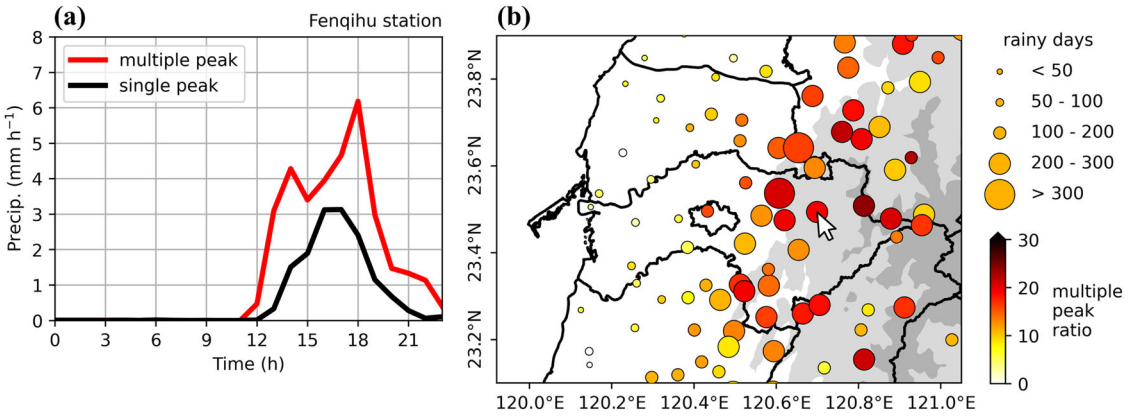


**Fig. 1 | Multiple-peak precipitation observed in southwestern Taiwan. a** The observed composite diurnal rainfall evolution over Fenqihu station (the white arrow in Fig. 1b) over the southwestern mountain areas of Taiwan when multiple rainfall peaks (red line, 51 days) or single rainfall peak (black line, 313 days) are detected in the daily precipitation time series. **b** The probability of detecting multiple rainfall peaks in the daily precipitation time series over southwestern Taiwan. The color of each circle shows the probability for each rain gauge station, while the size of the circle signifies the total count of rainfall days. The grey shadings represent the 500-m and 2000-m elevation contours, respectively. The statistics are based on Central Weather Administration hourly rain gauge observations during May-Sep., 1996–2020 for days not affected by strong synoptic weather systems (typhoons, fronts, strong southwesterly monsoon flows, or northeasterly flows).

diurnal cycle can be modulated by large-scale variability and future climate change.

In Taiwan, diurnal convection is most prevalent when the summertime Western Pacific Subtropical High (WPSH) covers the island[26]. Under this large-scale convectively suppressed condition, the initiation of the diurnal convection is primarily dominated by local circulation owing to differential heating of the terrain; thus, convection frequently occur over specific hotspots, leading to orographically-locked spatial patterns[26–29]. The configuration of the mountains and valleys constrains the flow of the sea-valley breeze, which modulates not only the initiation and propagation of convection[27] but also the non-local dynamics that supply moist static energy (MSE) to the precipitation hotspot through the low-level coherent flow[28]. To reveal the effects of topography or environmental variations, previous research has employed idealized experiments to explore their influences. For instance, Kuo and Wu (2019)[27] utilized conceptualized terrain configurations in their cloud-resolving (O ~ (500 m)) simulations to highlight the importance of local circulation on the initiation and development of afternoon convection in the Taipei Basin. Wu and Chen (2021)[24] conducted cloud-resolving experiments (O ~ (2 km)) to investigate the impact of changes in environmental humidity on convection over an idealized flat tropical island.

In the present work, we adopted the large-eddy simulation (LES) approach with a 100-m horizontal resolution so that the detailed evolution of boundary layer turbulence, the local circulation and the deep convection over an idealized ocean-plain-mountain terrain configuration can be explicitly resolved[30]. Inspired by the observations in Taiwan, our study will focus on the changes in thermodynamic environmental conditions first, by exploring how diurnal convection responds to free troposphere relative humidity (FTRH) under the scenario dominated by local circulation. The simulations are initialized with representative sounding observation features a typical environment under the large-scale suppression of summertime subtropical high-pressure system near Taiwan. As will be presented subsequently, the simulations reveal the existence of multiple peaks in the orographically-locked rainfall. We also perform sensitivity experiments, guided by the observed statistics in the soundings, to examine the response of the multiple-peak diurnal convection to different FTRH. In the control simulation, the RH at 500 hPa is set to 54%. Sensitivity experiments were conducted by adjusting the RH at 500 hPa to 34% in the drier simulation and 74% in the wetter simulation. We named these simulations RH34, RH54, and RH74 simulations, respectively. We conducted 5 ensemble members for each experiment by adding temperature perturbations at the lowest model level. Subsequent analyses will focus on one of these members. Consequently, we can assess the key physical processes during the diurnal development of local circulation and convection and their responses to the environmental impacts using these idealized experiments. The findings are expected to provide novel perspectives on understanding the diurnal convection in tropical regions under convectively suppressed large-scale conditions with a realistic range of ambient variability. The structures of convection, local circulation evolution, buoyancy relationships, and responses in convection-environment interactions to FTRH are analyzed in Section (Results). Section (Discussion) presents the discussions of the significance of multiple peaks, the non-local effect of MSE transport, and the implications of current findings. The model and sensitivity experiment setups are described in Section (Methods).

## Results

### Characteristics in Control (RH54) simulation

**Convection and local circulation evolution.** We first present the evolution of precipitation statistics, low-level circulation, and convective structures in the RH54 simulations to examine the possible processes modulating the diurnal convection. Figure 2a shows that more than 99.9% of the overall precipitation occurs in the mountain area and distributes nearly uniformly along the y-direction. This clearly demonstrates that the simulated convection systems are predominantly orographically locked. The time series of the mountain-averaged precipitation rate in Fig. 2b exhibits multiple peaks. The first two peaks are closely related to the evolution of sea breeze and valley breeze circulations (presented later), while the third peak is more dominated by the ice-phase microphysical process, and the fourth peak is relevant to the local circulation and boundary layer processes, such as cold pool interactions (as revealed in the animation in the Supplementary Material S1), exhibiting larger variabilities among ensemble members. The ensemble average precipitation rate in the second peak is 85% higher than the first peak (3.3 mm h$^{-1}$ vs. 1.8 mm h$^{-1}$). The precipitation spectra in Fig. 2c show that the extreme rainfall in the second peak of all members is also more enhanced than the first peak, as 99.9$^{th}$ percentile rainfall intensity increases from 40 mm h$^{-1}$ to 60 mm h$^{-1}$. The statistics are computed by generating the probability distribution function (PDF) from the temporal and spatial outputs at every grid point within the mountain area, considering each peak separately.

We note that the occurrence of the first precipitation peak is earlier than many diurnal cycle observations (such as Fig. 1). When using realistic terrain of the Taiwan island at 500-m resolution, VVM can successfully simulate the diurnal peak times and intensities that closely match the observations (see Fig. 1 in Chen et al.[29]), which demonstrated that VVM can

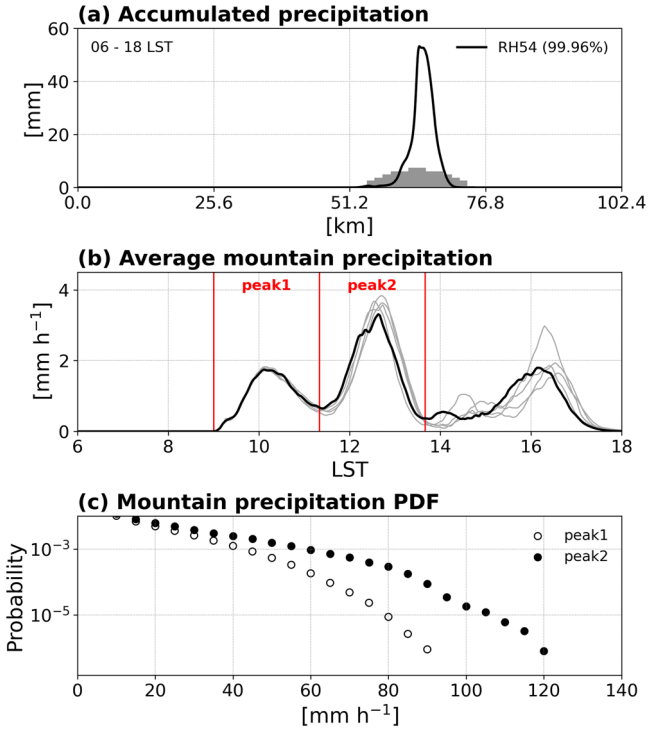


**Fig. 2 | Precipitation features of the RH54 (control) simulations. a** 12-hr accumulated precipitation. The upper right corner displays the ratio of mountain precipitation over total precipitation. **b** Mountain-averaged precipitation evolution. The black line represents one of the 5 ensemble members that we analyzed. The grey lines represent the other members. **c** Precipitation PDFs of the first two rainfall peaks. The open and closed dots represent the first and second rainfall peaks, respectively. In our simulation, we defined the time of the two peaks as 09:00–11:20 and 11:20–13:40.

capture the appropriate interactions of the physical processes for diurnal convection over terrain. Therefore, the earlier onset of precipitation presented here is likely due to the idealized terrain configuration, where the effects of surface heating may be more pronounced and lead to the earlier development of land-sea-mountain-valley breezes and convection initiation.

The ensembles of the simulation reveal that the first two rainfall peaks are the most robust features in the temporal evolution, while the subsequent peaks exhibit larger variabilities among ensemble members in their timing and amplitude. This indicates that the first two rainfall peaks are more directly responding to the background environment and locked to the development of the local circulation, and therefore will be the focus of this study. The latter peaks of convections are likely generated by convection-convection interactions or more complicated mechanisms and will not be analyzed in the present study.

Figure 3a shows the time evolutions of low-level circulation and boundary layer structures in one of the simulation members. Please note that the precipitation rate, low-level circulation, and boundary layer structures are averaged along the y-direction. At 9 AM of the simulation, sea breezes and valley breezes initiate individually over the coastline and mountaintop due to the disparate heating distributions caused by land-sea contrast and topographic differences. The first rainfall peak initiated between 9 and 10 AM owing to the convergence of valley breezes over the mountaintop. The averaged circulation and MSE distribution before the rainfall initiation (Fig. 3b, left panel) signify separated local circulation cells develop with a scale of O(10 km), with the inflow in the lower branch flowing towards the plain center (sea breeze) and towards the mountain top (valley breeze), respectively. From 10 AM to 12 PM (Fig. 3a), with the surface heating and the development of local circulation, MSE within the boundary layer increases, and the sea breezes progressively move inland and transport the low-level MSE into the mountain area. When sea breezes connect to valley breezes, the scale of the established local circulation is enlarged to approximately the scale of the island (Fig. 3b, right panel). The low-level inflow to the left of the mountain is also enhanced. The second rainfall peak initiated at around 11:30 AM and peaked at 12:30 AM with a stronger precipitation intensity than the first peak. In these two rainfall peaks, the depths of continuous inflow in the lower branch of the local circulation range from about 800 to 1200 m altitude.

Figure 4 displays the snapshots of updraft and convective structures at the peak time of the first two rainfall peaks (from the same member shown in Fig. 3). Note that the plot is zoomed in to the mountaintop. In the first rainfall peak, the sea breeze circulation is still separated from the valley breeze circulation, the weaker low-level inflow and updraft lead to lower convection development heights, weaker precipitation intensities, and narrower precipitation coverages. On the other hand, when the local circulation connects and covers the island in the second peak, there are stronger and wider updrafts that have more grids with vertical velocities exceeding 0.5 m s$^{-1}$. These updrafts can develop clouds with larger volumes, reaching a higher level of about 12-13 km in height. The second peak exhibits more significant cloud organizations, stronger precipitation intensity, and wider precipitation coverage, while the precipitation areas are positioned more to the right of the mountaintop.

The above analysis points out the significant differences in environmental and convective characteristics between the first two rainfall peaks. Moreover, both the clear structure of the sea breeze front propagating into the mountain (Fig. 3) and the vortices associated with a deep convection system (Fig. 4) over the simulation can be well resolved at a 100-m resolution. To gain a more in-depth understanding, we further analyze the two rainfall peaks separately.

**Relating Buoyancy, CAPE and Upstream MSE Transport**. The two distinct rainfall peaks exhibit significant differences in precipitation intensity and convective characteristics. We attribute these distinctions to the non-local dynamics effect that entrains MSE transported by local circulation, as previously discussed by Chang et al. (2023)[28]. They indicated that for orographically locked diurnal convection, local circulation plays a crucial role in continuously supplying the required energy and intensifying convection. To understand how differences in the two rainfall peaks are influenced by energy transport from the upstream, our specific focus is on the "precipitation hotspots". These hotspots are defined as columns with both strong updrafts and high precipitation intensities (see Supplementary Material S2 for details).

Recognizing the vital role of buoyancy as a key variable for quantifying the impact of environmental thermodynamic factors on convective intensity and its general positive correlation with precipitation intensity[31–33], we have selected buoyancy as the diagnostic variable to investigate the convection-environment interaction. Figure 5a shows the correlation analysis between 3-10 km average buoyancy strength and precipitation intensity. Here, buoyancy is defined as:

$$\text{Buoyancy (B)} = g\frac{\theta_v - \bar{\theta}_v}{\bar{\theta}_v}[ms^{-2}] \quad (1)$$

where $g$ is gravity acceleration and $\theta_v$ is virtual potential temperature. The overbar represents the average over the environment. Note that the size of the environment used for buoyancy calculations will change according to the scale of the convective systems. The environment influencing buoyancy strength encompasses every nearby grid point, regardless of whether it is raining or if the convective region belongs to other systems. A smaller region of the environment is used for the first peak (about 3-km in diameter) and a larger one is used for the second peak (about 10-km in diameter). There are stronger buoyancy strengths in the second rainfall peak compared to the first peak. Significant positive relationships exist between buoyancy and precipitation intensity in both the first two rainfall peaks, with correlation coefficients of 0.69 and 0.66, respectively. Note that the value of averaged

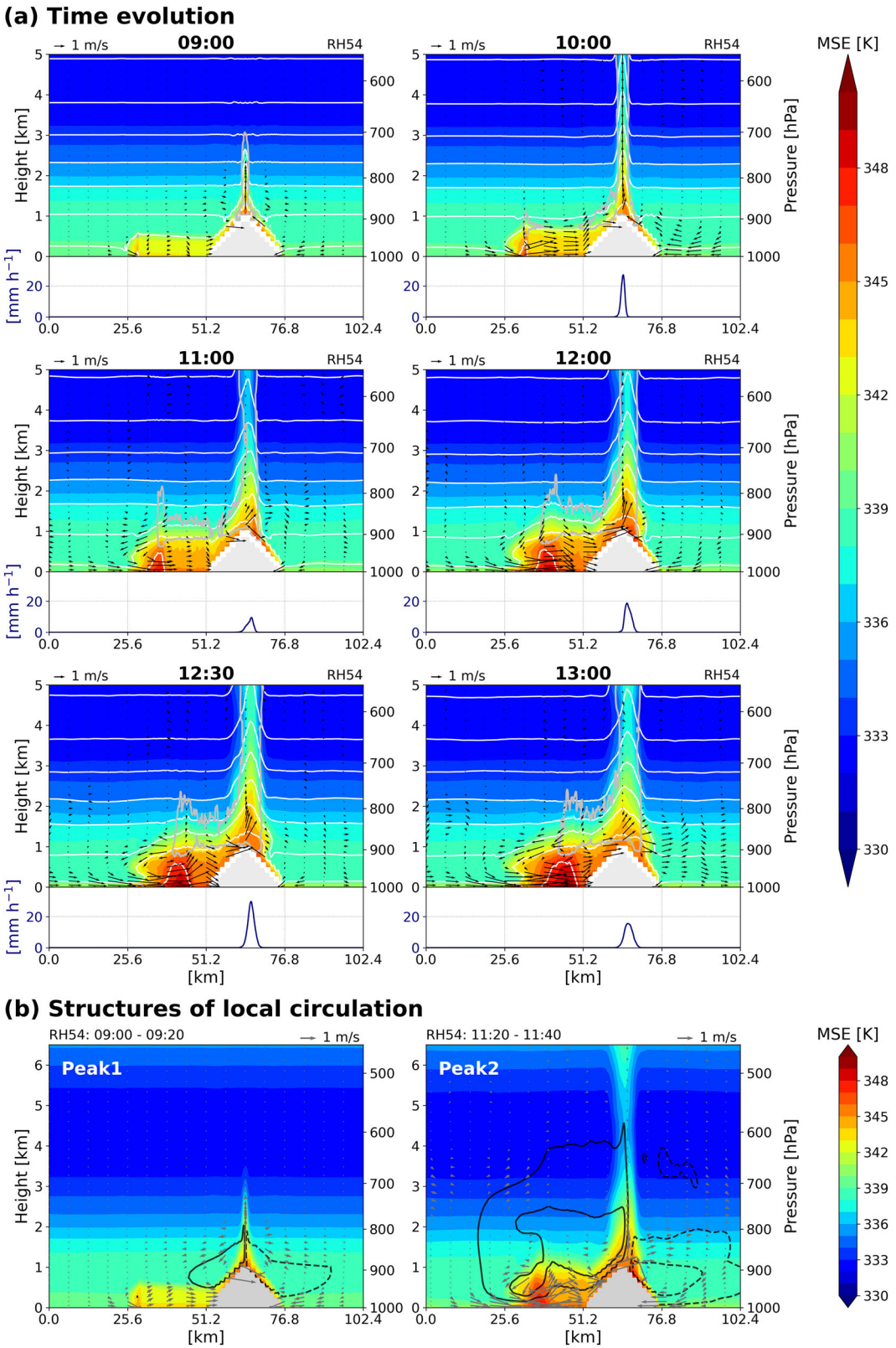


**Fig. 3 | Local circulation and boundary layer structure. a** Time evolution of low-level local circulation and boundary layer structure averaged along the y-direction. The color shading represents MSE. The white contours represent specific humidity (the interval is 2 g kg$^{-1}$). The grey contours represent clouds, which are defined as hydrometeors with a concentration of at least $10^{-5}$ kg kg$^{-1}$. The quivers represent u- and w-component wind fields. The blue lines represent the precipitation rate. **b** The MSE distribution (shading), stream function (contour; the interval is 800 m$^2$ s$^{-1}$), and u- and w-winds (quivers) averaged along the y-direction in the RH54 simulation before the first (left panel) and the second (right panel) rainfall peaks, respectively.

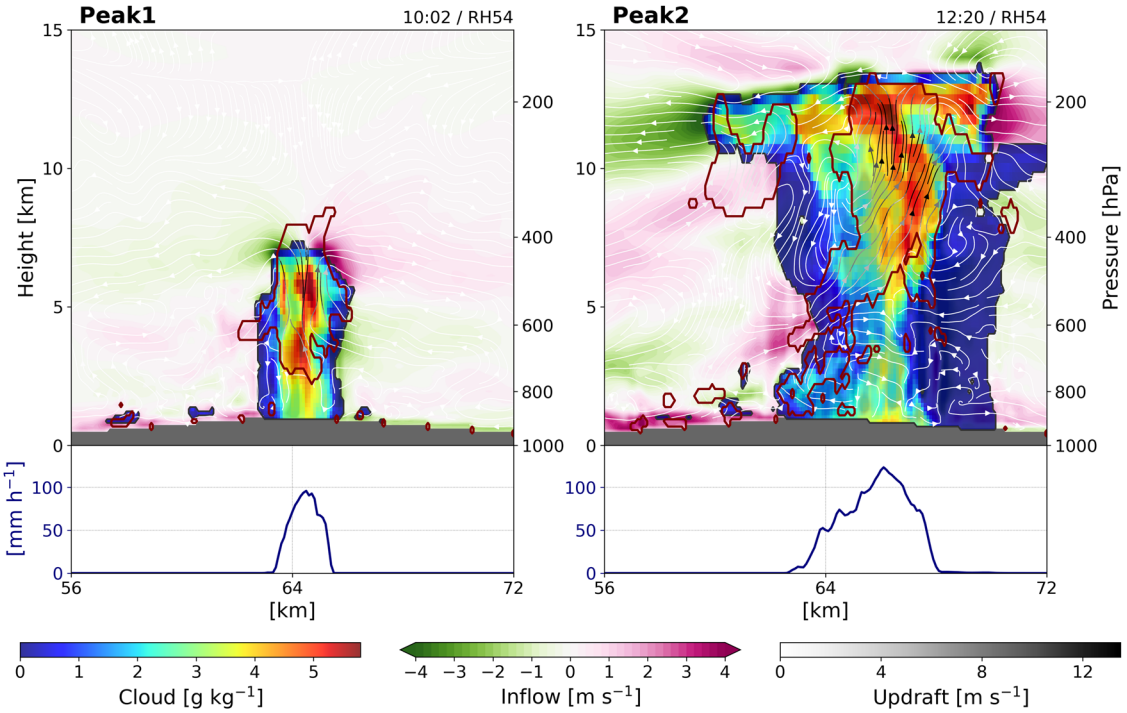


**Fig. 4 | Snapshots of cloud structure, wind field, and precipitation near the mountain top.** The left and the right panel represent the first and the second rainfall peaks, respectively. The rainbow shading represents the total hydrometeor concentration in clouds. The pink-green shading and streamlines represent the u- and w-component wind, respectively, with darker colors indicating stronger wind speed. The red contours represent updrafts larger than 0.5 m s$^{-1}$. The blue lines in the bottom represent the spatial distribution of precipitation rate.

buoyancy strength is slightly negative with overall neutral conditions. This is because some columns with negative averaged buoyancy are still included when the vertical velocity begins to weaken, but not weak enough to be excluded from the definition of convective columns (Supplementary Material S2).

However, buoyancy is challenging to directly observe in the real world. To address this limitation, we utilize measurable variables such as entraining convective available potential energy (CAPE) and low-level MSE transport as potential indicators for convective buoyancy. By examining their relationship with precipitation intensity, we can gain insights into the pivotal factors influencing buoyancy strength and precipitation intensity. Figure 5b first examines how precipitation intensity is related to entraining CAPE one hour before precipitation occurs, defined as:

$$\text{Entraining CAPE} \equiv \int_{h_{mp}-h_{ms}>0} R_d(h_{mp}-h_{ms})d\,lnP \qquad (2)$$

where $R_d$ is the gas constant for dry air, $h_{mp}$ is the MSE of an entraining parcel from the surface with the parcel evolution model based on a constant entrainment rate: $dh_{mp}/dz = -\varepsilon(h_{mp}-h_{ms})$ and $\varepsilon$ is set to $10^{-4}$ m$^{-1}$. The constant entrainment rate is based on the smaller entrainment rate observed in rapidly developing deep convection[34]. $h_{ms}$ is the saturated MSE, and $P$ is the pressure. The results show that there is a positive correlation ($R = 0.33$) during the first rainfall peak between precipitation intensity and the entraining CAPE over the precipitation hotspot, while such a relationship is weakened ($R = 0.14$) during the second peak, suggesting that CAPE, the initial background environment, is responsible for the precipitation intensity in the first peak rather than the second peak. As precipitation occurs, CAPE decreases due to the environment adjusting towards a moist adiabatic state. This results in negative correlations between CAPE and precipitation intensity ($R$ = -0.39 and -0.14; figure not shown).

For the second diurnal precipitation peak, we hypothesize that the upstream MSE transported by local circulation is an important source of convective buoyancy, as the circulation is well established at a larger scale prior to the second precipitation peak. As demonstrated in Fig. 3b, the lower branch of circulation provides a coherent flow, which effectively transports upstream low-level high MSE into convective regions. Thus, we quantified the local circulation-driven low-level upstream MSE transport, called "upstream MSE", which is the summation of the low-level-integrated MSE flux within the upstream 20 km (see Supplementary Material S3 for the details). The low-level-integrated MSE flux is defined as:

$$\text{Low–level–integrated MSE flux} \equiv \int_{sfc}^{Z} h_m V\,dz \qquad (3)$$

where $Z$ is the top of the continuous u-wind that exceeds 0.1 m s$^{-1}$ below 3 km (about 800–1200 m), $\boldsymbol{V}$ is u-wind, and $z$ is height. Here, we take the rightward as positive.

Figure 5c shows the relationship between precipitation intensity and the upstream MSE. They are positively correlated in the second peak ($R = 0.27$), and this positive relationship is statistically significant. However, there is no correlation in the first rainfall peak ($R = -0.09$). This suggests that low-level upstream MSE transport, driven by local circulation, efficiently strengthens the precipitation in the second peak and becomes the dominant energy supply for buoyancy. The results suggest that the differences in the characteristics of the two rainfall peaks are linked to the relative contribution of non-local energy transport to the buoyancy of the convection near the mountaintop. Local circulation plays a pivotal role in conveying MSE from upstream, serving as a critical source of convective buoyancy enhancement in the second peak. This process significantly contributes to rainfall extremes.

### Sensitivity to free-troposphere moisture

**Response in convection-environment interactions.** As the dominant buoyancy sources are different between the first and second rainfall peaks, they may exhibit different responses to the environmental conditions. We postulate that the first rainfall peak, which is directly controlled by CAPE, may be enhanced when the mid-level environment

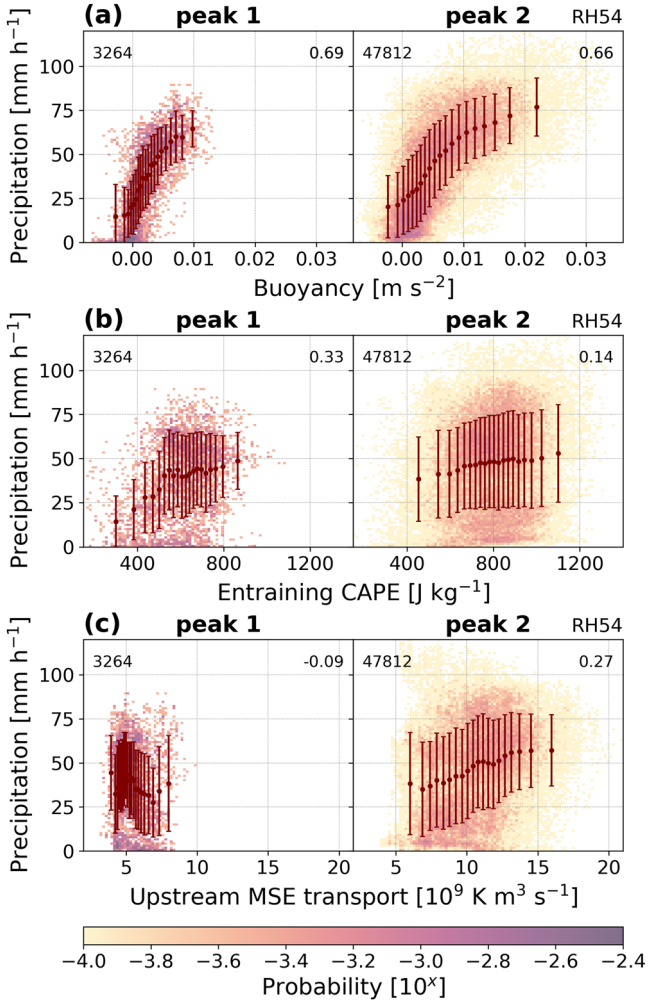


**Fig. 5 | Relationships between precipitation intensity and buoyancy, entraining CAPE, and upstream MSE transport. a** The relationships between precipitation intensity and local buoyancy over the precipitation hotspots during the first (left) and the second (right) rainfall peaks of the RH54 simulation. The values in the upper left and right corners represent the sample sizes and correlation coefficients, respectively. **b** similar to (**a**) but the relationships between precipitation intensity and entraining CAPE (see Section "Relating Buoyancy, CAPE and Upstream MSE Transport" for definition) one hour before precipitation occurs. **c** similar to (**b**) but the relationships between precipitation intensity and upstream MSE within 20 km from the precipitation hotspots. These correlations passed the t-tests and are statistically significant at the 95% confidence level.

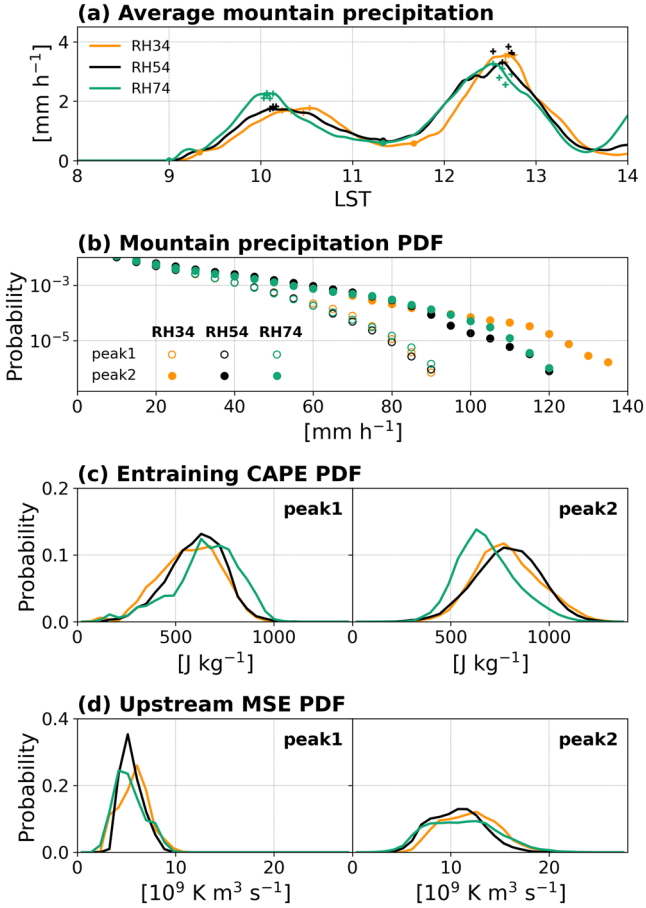


**Fig. 6 | Precipitation evolutions and PDFs of precipitation, entraining CAPE, and upstream MSE transport of sensitivity experiments. a** Same as Fig. 2b but for one member each of the RH34 (orange), RH54 (black), and RH74 (green) simulations. The dots represent the initiation times of the first two rainfall peaks. The plus markers represent the maximum precipitation rate of each ensemble member in each peak. **b** Same as Fig. 2c but for all simulations. **c** PDFs of entraining CAPE one hour before precipitation occurs for one of the ensemble members over the precipitation hotspots during the first two rainfall peaks. The solid and dashed lines represent the first and the second peaks, respectively. **d** Same as (**c**) but for upstream MSE.

becomes wetter. As the second rainfall peak is association more strongly with upstream MSE transport, if the MSE distribution and the local circulation before its onset is modulated differently by the earlier convection, the intensity of the second rainfall peak can yield the opposite response to initial moisture conditions. The following analyses on the sensitivity experiments will focus on revealing these detailed mechanisms.

Figure 6a shows that, regardless of changes in the free troposphere moisture, the precipitation characteristics exhibit similar mountain-averaged precipitation evolutions between the RH34, RH54, and RH74 ensemble simulations during the first two rainfall peaks. The drier (RH34) simulation experiences a 20-min delay in precipitation development during the second peak. Furthermore, the precipitation intensity spectra (Fig. 6b) indicate that more extreme precipitation occurs in the drier (RH34) ensembles during the second peak. Figures 6c, d illustrate the PDFs of entraining CAPE and upstream MSE over the precipitation hotspots within the first two rainfall peaks. According to the analyses in Section (Relating Buoyancy, CAPE and Upstream MSE Transport), convection intensity is dominated by entraining CAPE and upstream MSE during the first and the second rainfall peaks, respectively. Due to less dry environmental air being entrained into surface air parcels in the wetter (RH74) simulation, there is higher entraining CAPE and consequently stronger precipitation intensity in the first peak. On the other hand, in the drier (RH34) simulation with higher upstream MSE, there is stronger precipitation intensity in the second peak. This raises the question of why the two peaks exhibit opposite dependence on moisture.

In the first rainfall peak, the intensity of average mountain precipitation demonstrates the dependence on environmental humidity. However, this mechanism is not significant in the second peak due to the modification of the background environment over the mountaintop. Due to the development of the boundary layer and the occurrence of the first rainfall peak, there are notable changes in the profiles of RH (Fig. 7a) and MSE (Fig. 7b). The increase in near-surface temperature leads to elevated MSE near the surface, while RH decreases in the plain area. The decrease in MSE at 800 hPa can be attributed to the subsidence in the surrounding environment. By the convection during the first peak, the environment undergoes humidification and upward transport of MSE, causing an increase in both RH and MSE in the upper

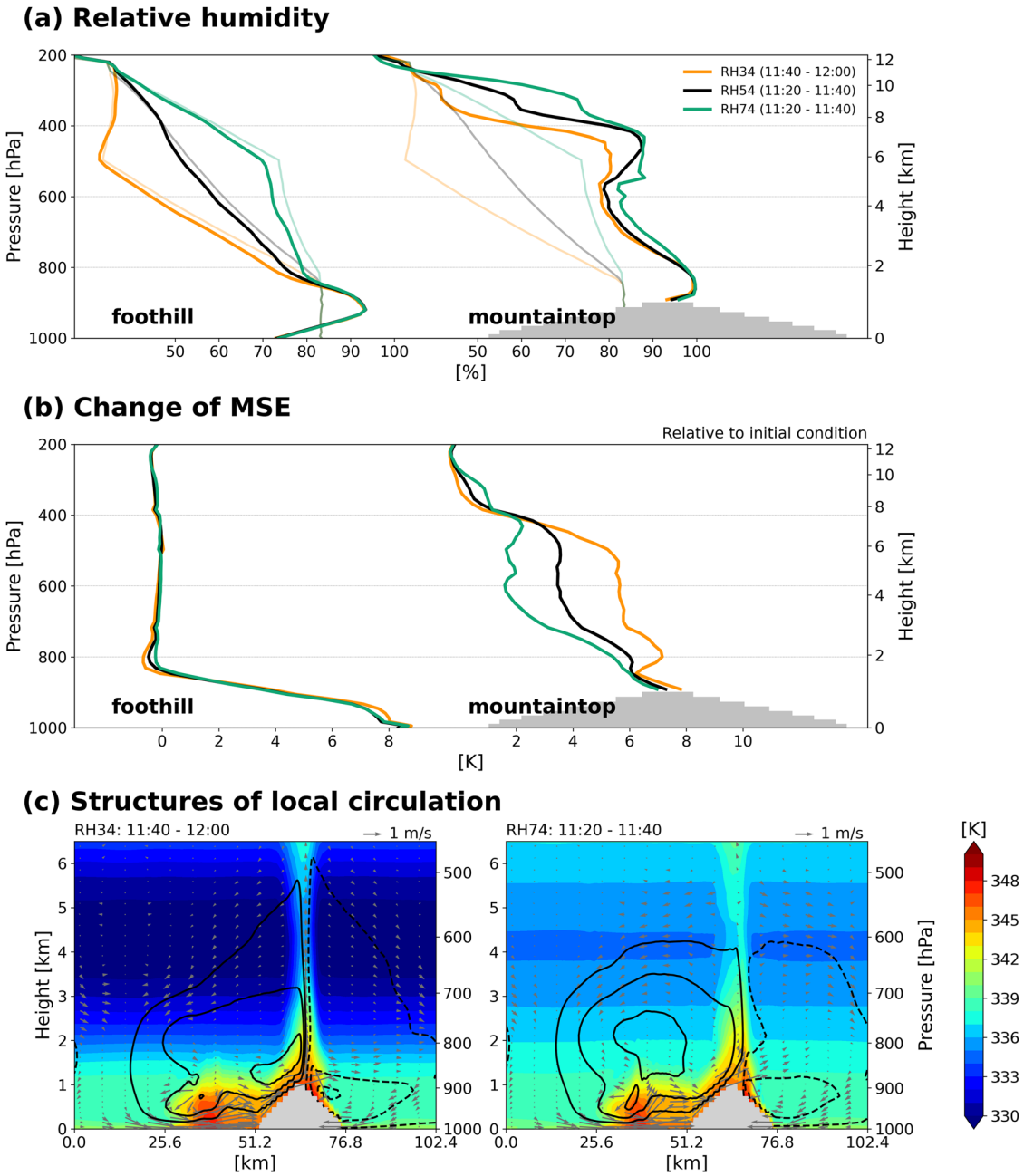


**Fig. 7 | Changes of relative humidity, MSE, and local circulation structure after the first peak. a** RH profiles before the second peak in the RH34 (orange), RH54 (black), and RH74 (green) simulations. The left and the right represent the foothill and the mountaintop. The light-colored lines represent the initial RH (6 AM). **b** Same as **a** but for changes in MSE from the initial state to the time after the first peak. **c** Same as Fig. 3b but for the RH34 (left) and the RH74 (right) simulations before the second peak.

troposphere. This convective adjustment modifies the environmental conditions over the mountaintop. As a result, the environmental discrepancies between the RH34, RH54, and RH74 simulations become less pronounced after the occurrence of the first rainfall peak at the mountaintop. Even though the mountaintop environment is adjusted to similar profiles before the second rainfall peak, the low-level MSE transport has pronounced differences among sensitivity experiments during the second peak (Fig. 6d). Figure 7c shows that a stronger and more circular-like circulation structure is shown in the wetter (RH74) simulation. In contrast, a terrain-following structure is observed in the drier (RH34) simulation prior to the second rainfall peak. The inflow in the lower branch of local circulation is stronger in the drier (RH34) simulation due to the delayed precipitation evolution and the prolonged development of local circulation. The spatial distribution of MSE and the structure of the local circulation cell both play important roles in modulating the overall MSE transport.

**Response of MSE budget of the second rainfall peak.** To clarify the contribution of local circulation-driven upstream MSE transport to convection strength in the second rainfall peak, we carried out an MSE budget analysis by separating the boundary layer and free troposphere (see Supplementary Material S4 for details). This analysis focuses on the mean flux advection term along the x-direction $-\frac{\partial \overline{uh}_m}{\partial x}$ to emphasize the importance of the lower branch of the local circulation. This MSE budget analysis provides a quantitative understanding of the primary layers that contribute to the energy required for convection under different

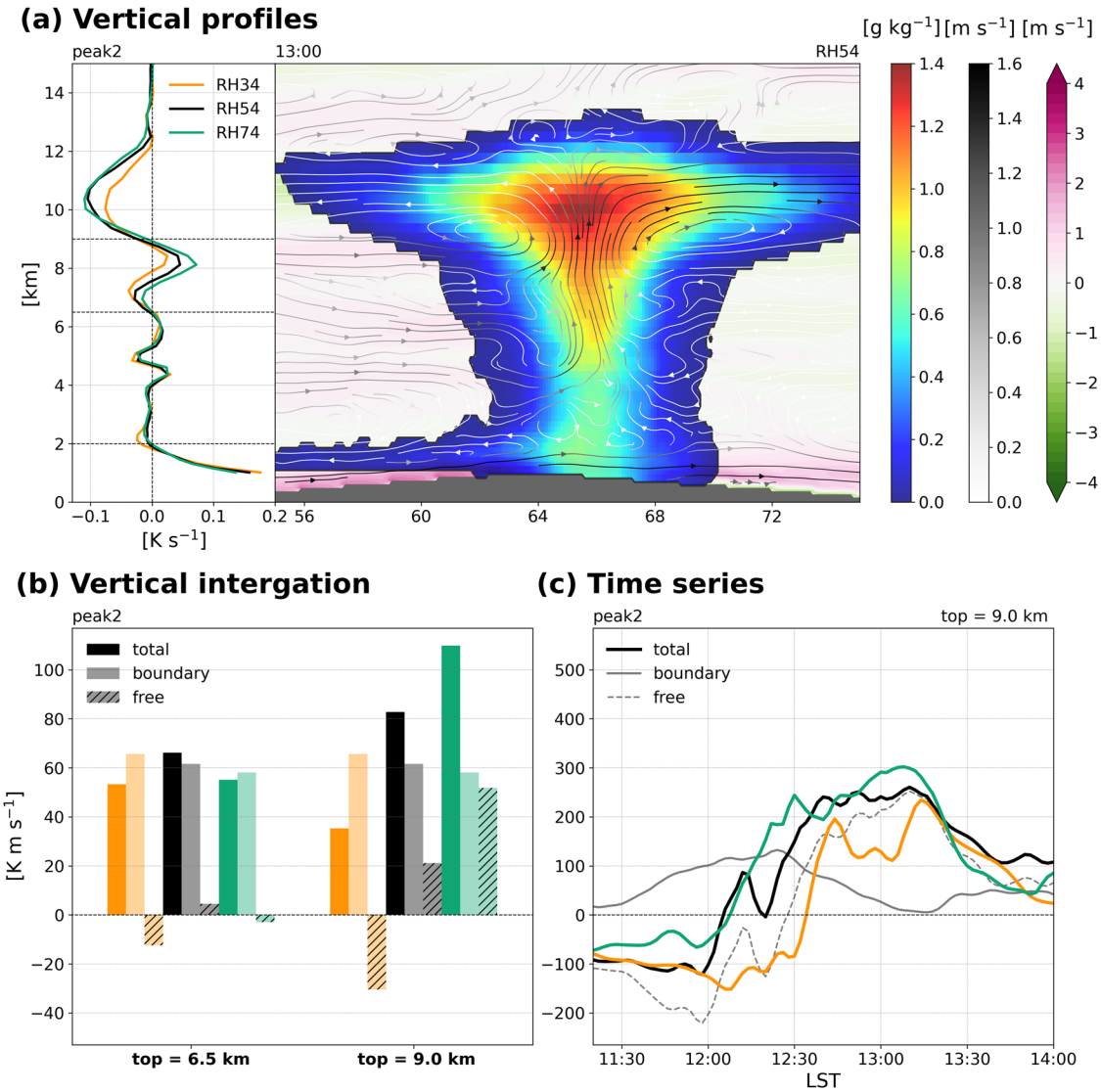


**Fig. 8 | MSE budget analysis. a** The left panel shows vertical profiles of the mean flow advection of MSE averaged over the second rainfall peak. The right panel shows the vertical structure of convection, same as Fig. 4 but averaged along the y-direction in the RH54 simulation. The streamlines represent the wind speed. **b** Vertical-integrated MSE advection of mean flow. The boundary layer is defined from the surface to 2-km height. The free troposphere is defined as 2 km to 6.5 and 2 km to 9 km, respectively. **c** Time series of vertical-integrated MSE advection. The thicker, thinner, and dashed lines represent the integration of the total troposphere, boundary layer, and free troposphere, respectively, with the top of the free troposphere defined as 9 km.

environmental conditions. This is valuable for the subsequent research on the non-local effects of convection (discussed later). The vertical profiles of MSE advection in Fig. 8a indicate the presence of strong coherent MSE inflows at the lower levels and at approximately 8 km height. The low-level coherent MSE inflow is driven by the lower branch of the local circulation, while the upper coherent MSE inflow is associated with the anvil cloud outflow.

We defined the boundary layer from the surface to 2 km height and the two layers of free troposphere from 2 to 6.5 km and from 2 to 9 km based on the flow structure. By vertically integrating the MSE advection, we aimed to identify the role of dynamic entrainment from the free troposphere. Figure 8b reveals that the magnitudes of vertically integrated free troposphere MSE advection are larger when the top of the free troposphere is defined as 9 km, suggesting the upper coherent MSE inflow contributes to sources of MSE. The free troposphere and total MSE advection increase when the free troposphere becomes wetter. Conversely, the boundary layer MSE advection decreases with increased moisture in the free troposphere. Therefore, convection development relies more on low-level MSE transport in the drier (RH34) simulation. Additionally, the time series of MSE advection (Fig. 8c) shows significant delays in the drier (RH34) simulation. The peak of boundary layer MSE advection precedes the peak of the free troposphere and total MSE advection, as the latter is mainly attributed to the upper-level MSE coherent flow occurring at the later mature stage of convection.

These results highlight that the content of background MSE in the free troposphere, as well as the structure and development of local circulation, significantly affect the required energy supply and the strength of diurnal convection.

## Summary and future outlook

This study investigates detailed evolution of the diurnal convection under local circulations dominant environment over a conceptualized tropical mountainous island using idealized LESs, providing a novel perspective on the convection-environment interactions and energy transport by local circulation with varying environmental characteristics. We utilized the Vector Vorticity equation cloud-resolving Model (VVM) with high spatial and temporal resolutions to capture the detailed evolution of the turbulent boundary layer and convection driven by horizontal buoyancy inhomogeneity. By environmental conditions from observations in Taiwan over the

conceptualized terrain configuration, we established a general framework for understanding the physical processes modulating the multiple rainfall peaks in the orographically locked diurnal convection. The first two simulated precipitation peaks are robust and closely related to the evolution of local circulation. The convection in first rainfall peak is a direct response to the environmental stability (CAPE) and triggered by the convergence of valley winds at the mountain ridge. In the second rainfall peak, with the local circulation in the island scale and weaker free troposphere entrainment, upstream MSE is transported into convection through a 1-km depth inflow. This process leads to more extreme precipitation and higher degrees of cloud organization compared to the first peak. Modifying the FTRH changes the contribution of low-level upstream MSE transport to convective buoyancy in two ways. First, it affects the scales and structures of local circulation. In the drier simulation, the prolonged development and the terrain-following structure of local circulation increase the upstream MSE transport. Second, it influences the free troposphere background MSE, which impacts the entrainment of MSE. The MSE budget analysis demonstrates that the main MSE transport is dominated, particularly in the RH34 simulation, by a coherent inflow associated with the local circulation. However, there is detrainment of MSE in the free troposphere in the RH34 simulation, whereas the RH54 and RH74 simulations still have MSE entrainment. Therefore, the higher reliance on boundary layer MSE supply in the RH34 simulation leads to a more significant enhancement of convection strength through the increased MSE transport.

In this study, we have been able to distinguish the unique characteristics of diurnal convection over tropical islands during each rainfall peak and in varying environmental conditions through the application of LES using idealized VVM simulations. We conclude that the non-local dynamics in entraining upstream MSE plays a crucial role in extreme rainfall. The redistribution of moisture during the earlier precipitation peak creates a more conducive environment for later convection development, magnifying the influence of low-level upstream MSE transport and reducing the impact of free troposphere entrainment on estimating convection strength. Besides, the local circulation, driven not only by land-sea differences and complex topography but also by the secondary circulation induced by the earlier precipitation, effectively transports MSE from upstream areas to the mountain region. The contribution of upstream MSE transport depends on the scale and the structure of the local circulation establishment.

Our research reveals that under complex topography, the spatio-temporal details of convective development arise from the coupled interactions between thermodynamic and dynamic processes. Consequently, under the local circulation dominant specific regime in this study, two crucial points in climatology, CAPE, and environmental humidity, cannot solely explain the convective strength. Instead, we find that convective strengths are significantly influenced by energy transport from the environment—the mutual interaction between thermodynamic conditions and dynamic processes—rather than being determined by only the state of the local surface parcel.

This study establishes the conceptual mechanism that can be extended to potential applications in further experiments by simulations and field observations. By conducting various sensitivity experiments—such as changing the land type or introducing background wind with a mountainous island surrounded by ocean—we can gain insights into the variability and complexity of local circulation, exploring dominant processes behind it. For example, the balance between the cold pool and environmental shear in the west-east direction[35,36] may impact circulation and convection intensity, which warrants further investigation in future studies. Additionally, sensitivity experiments involving modifications to the scale and shape of the island will also be valuable in the future. These could help extend the framework in this study to various tropical islands. Furthermore, these findings can inform the strategies for field observation, helping us to better capture and understand the physical processes occurring in the real world. For instance, the MSE budget analysis highlights the features of upstream energy transport, such as the depth of low-level energy inflow. This research not only advances our theoretical understanding but also provides practical guidance for future observational and experimental efforts.

## Discussion

In the past, many studies have described diurnal convection either by presenting only a single peak or through statistically analyzing the strongest or longest-lasting peak. However, multiple precipitation peaks exist over the complex topography such as in Taiwan. Convection rapidly redistributes the environmental energy through circulation, and on the other hand, the impact of the environmental conditions on different rainfall peaks varies accordingly. Therefore, assuming a single diurnal rainfall peak can overlook the mechanisms behind and sensitivities of each rainfall peak. Incorrect assessment of diurnal convection-environment interaction can lead to erroneous estimates when investigating potential changes in convection under intraseasonal or future climate conditions, especially concerning variations in extreme precipitation. Our study highlights the significance of multiple rainfall peaks under a local circulation-dominant environmental regime. We found that the sensitivity of convection-environmental interaction differs between the first two robust peaks, leading to varying environmental factors influencing convective intensity. While the convection during the first rainfall peak can be determined by a simple thermodynamic factor, such as CAPE, the convection during the second peak necessitates simultaneous consideration of both thermodynamic and dynamic effects.

To augment the robustness of the key findings in the present studies, especially the influence of the first rainfall peak on the second peak, here we conducted two additional experiments by zeroing out CAPE in the initial conditions to suppress the first rainfall peak. The initial low-level RH, which is 83% in the control (RH54) simulation, is reduced to 75% (nocape75) and 67% (nocape67), respectively (Supplementary Material Figure S8). The temporal evolution of the mountain-averaged precipitation intensity in these two no-CAPE experiments are shown in Fig. 9a. The first two peaks remain evident in the nocape75 experiment, highlighting the robustness of the multiple-peak feature under this terrain configuration. To effectively suppress the first peak requires a substantial reduction in initial low-level RH as in the nocape67 experiment. In this case, the "second peak" — supported by energy from local circulation — is also drastically weakened and delayed. Figure 9b compares the changes in RH profiles over the mountainous region. After the first rainfall peak in the nocape75 experiment, the free-troposphere environment over the mountains is moistened. In contrast, in the nocape67 experiment, with the first peak being absent, the FTRH remains below 60%. This supports that convection of the first rainfall peak moistens the free troposphere over the mountainous region, which is part of the reason that the second peak is less sensitive to the initially drier FTRH. Furthermore, in the nocape67 experiment, a noticeable island-scale local circulation still exists (see Supplementary Material Figure S9) and supports the occurrence of the rainfall peak, although with a shallower structure. The drier low-level RH leads to reduced boundary layer MSE, which results in a much weaker upstream MSE supply in nocape67 experiment in contrast to the control (RH54) simulation. This supports that the intensity of the second peak is highly associated with the energy transport by the low-level branch of the local circulation cell. We note that the control experimental design was guided by the summertime environment of afternoon thunderstorms in Taiwan, which is characterized by a high low-level RH ( > 80%) within the tropical marine boundary layer. The purpose of these no-CAPE experiments here is to intentionally suppress the first rainfall peak and reveal its impact. Quantifying and evaluating the contribution of the first peak on developing the second peak can be the focus of future work.

Upstream MSE and its variability plays a crucial role in estimating convective intensity during the second peak. The specific mechanisms of upstream MSE supply driving increased extreme precipitation are essential for helping us understand the importance of dynamic processes. A possible process is that the increase in MSE transport leads to enhanced buoyancy strength, which impacts the strength of updrafts and the overall structure of convection. We suppose that the low-level upstream MSE transport plays a

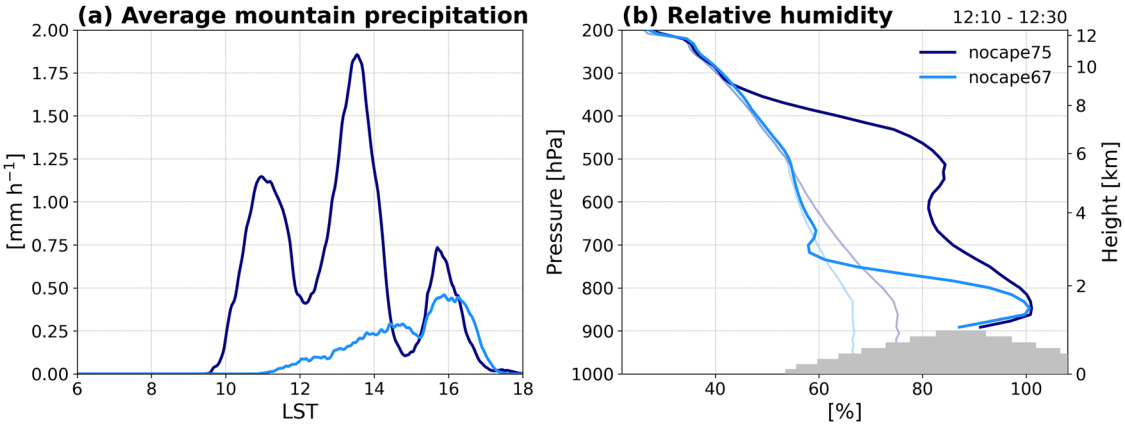


**Fig. 9 | Results of no-CAPE sensitivity experiments. a** Mountain-averaged precipitation evolution. The dark blue and sky blue lines represent the nocape75 and nocape67 simulations, respectively. **b** RH profiles before the second peak in the nocape75 (dark blue) and nocape67 (sky blue) simulations over the mountaintop. The light-colored lines represent the initial RH (6 AM).

more crucial role in this process. This hypothesis is supported by the MSE budget analysis, which reveals that in the RH74 simulation during the second rainfall peak, there is a greater MSE transport by the mean-flow from 6.5 km to 9 km, but there is no significant increase in precipitation intensity. This may be attributed to that the low-level branch of circulation can drive the more effective enhancement of vertical MSE transport within the convective system, contributing to the increase in the occurrence of extreme rainfall by altering the convection structure. This relationship may be associated with changes in the intensity and spatial coverage of convective buoyancy. The circulation structure, influenced by buoyancy and their corresponding non-local effects, can impact the convection organization. Additionally, the strength of cold pools and their interaction with the environment could contribute to the increase in extreme rainfall events. Variations in the intensity, thickness, and depth of cold pools under changing environmental conditions may also influence convective triggering. Therefore, our future focus will involve a more in-depth analysis of convective buoyancy characteristics and cold pool dynamics.

Through the idealized ocean-plain-mountain terrain configuration employed in our study, we successfully simulated the complexity of diurnal convection, including the multiple-peak diurnal precipitation evolution observed in the real world, and investigated the mechanisms determining the intensity of each precipitation peak. This led to discussions regarding the applications of our current results with convection over the realistic complex topography of Taiwan Island. We can utilize the TaiwanVVM[37] framework with high-resolution Taiwan topography, applying the mechanisms demonstrated in this study to real complex topography[26,28,29,38,39]. This provides the possibility of more detailed analyses at locations where multiple precipitation peaks are observed, exploring the scales and structures of local circulation on real topography. Additionally, this allows us to explore whether the contributions remain the same under varying environmental conditions when the pathways of MSE transport driven by local circulation are no longer consistent. Furthermore, observations by Chang et al. (2023)[28] using the Storm Tracker mini-radiosondes[40] in the southern region of Yilan have revealed an increase and thickening of MSE transport within the boundary layer over time. For future applications in observations, we can deploy radiosondes at different distances from the precipitation hotspots to observe variations in MSE transport with distance, thereby further analyzing changes in the structure of local circulation and MSE transport in response to varying environmental conditions.

## Methods

### The Vector Vorticity Equation Cloud-Resolving Model (VVM)

To investigate the diurnal convection under local circulation dominant environmental conditions over an idealized terrain configuration, the Vector Vorticity Equation Cloud-Resolving Model (VVM)[37,41,42] is used in this study. The VVM was developed by Jung and Arakawa (2008)[41] based on the three-dimensional anelastic vorticity equations in height coordinate, in which the pressure gradient force is eliminated. In VVM, the horizontal vorticity is one of the prognostic variables and the vertical velocity is diagnosed by solving a 3-D elliptic equation. This approach demonstrates the one-to-one relationship between buoyancy and horizontal vorticity that allows the direct response of the surface fluxes. It can better capture the local-scale circulations caused by a strong horizontal buoyancy gradient, such as land-sea-mountain-valley breezes and cold pool fronts[37]. The model top is a rigid lid with gravity wave damping. The orographic effect is treated by imposing vorticity at the corner of the block mountains[42,43] to satisfy kinematic boundary conditions. Turbulence is explicitly simulated in VVM, allowing the resolved vorticities to interact with other physical processes, while the stability and deformation-dependent mixing is parameterized as a sub-grid process for the eddy viscosity and diffusivity coefficients[44]. With the high spatial resolution (100 m), the large eddies generated by the terrain heating, convective-scale dynamics and the turbulent flows of the land-sea-mountain-valley breezes circulation developed over the terrain are explicitly simulated and well resolved. The vorticity formulation, together with the implementation of Noah land surface model (Noah LSM v 3.4.1)[45,46] and Predicted particle properties (P3) scheme[47], enables the model to effectively represent the local circulation and the subsequent convection generated by differential surface heating over complex, steep topography. Past studies have demonstrated the advantages of VVM to investigate convection-environment interactions for various scales and topographical configurations. The model well represents the key processes modulating local circulation on afternoon thunderstorms in the idealized Taipei Basin[27] and realistic Taiwan island[28], the impact of land-atmosphere interactions over idealized tropical islands[24], the effects of microphysics on extreme precipitation over the ocean[48] and over complex topography[26], and the development of convection over the ocean[49–53].

### Model Configuration and Experiment Design

In this study, we applied an idealized terrain configuration and specific environmental conditions to emphasize the physical processes and environmental characteristics of a particular convection type. Taking inspiration from the topography in Taiwan, where the first row of the mountain range has an approximate height of 1 km, an idealized terrain configuration is applied in a 102.4 × 102.4 km domain size, which includes ocean (51.2-km width), plain (25.6-km width), and mountain (25.6-km width and 1-km height) in the x-direction and uniformly in the y-direction (Fig. 10b). It can be regarded as a mountainous island with a triangular shape in the x-z cross-section by applying doubly periodic boundary conditions, which similar to the configuration used in Chen et al., (2019)[50] to study the development of diurnal convection over coastal ocean of tropical mountainous islands. Since

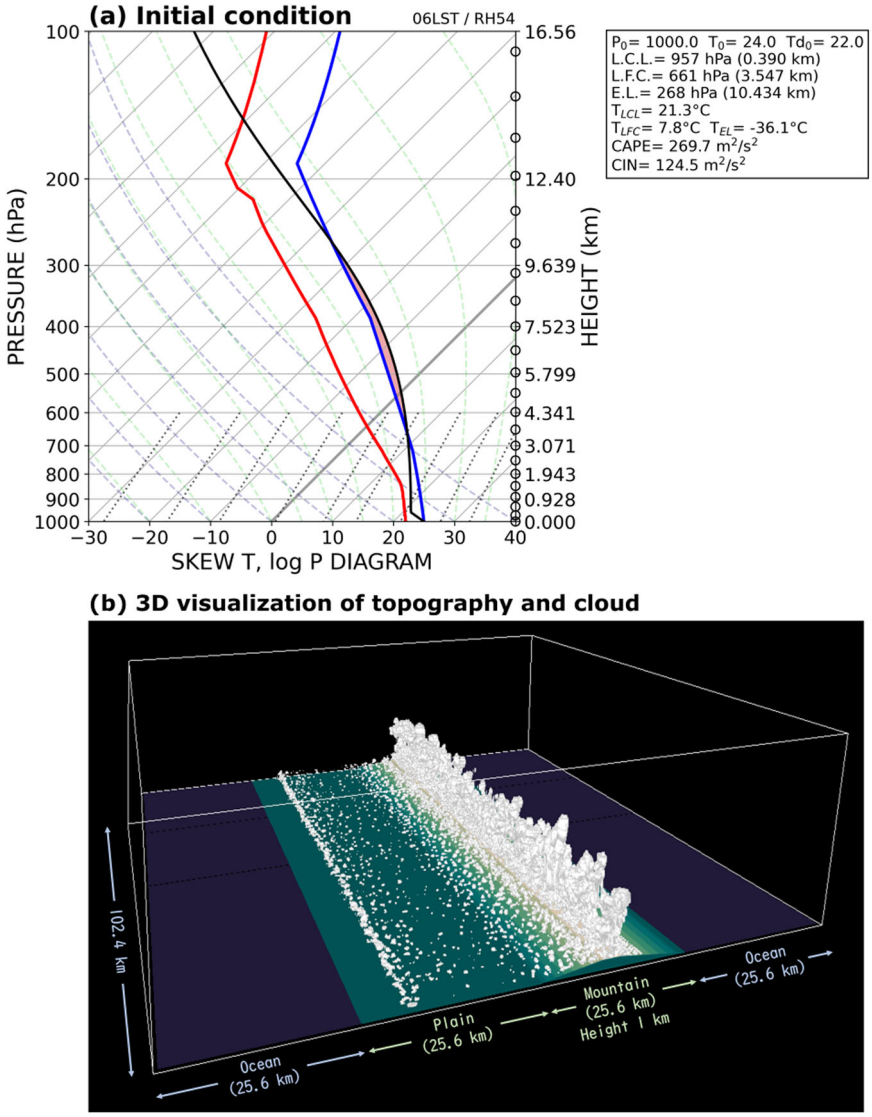


**Fig. 10 | Model Configuration. a** Initial environmental vertical profile of the control (RH54) simulation presented as a SKEW-T log-P diagram. The blue and red lines represent temperature and dew point temperatures, respectively. The black line represents the temperature of the air parcel as it lifts pseudo-adiabatically from the surface. The shaded area represents CAPE. **b** The idealized terrain configuration of the LESs. The blue and green patches represent the ocean and land regions, respectively. The land region includes plain and mountain, with the mountain height of 1 km.

we aim to explore the interactions between the land-sea-mountain-valley breezes and orographically locked convection first, this configuration simplifies the complexity of local circulation structures by emphasizing the variations in circulation and diurnal convection in the x-direction. The land surface type we use is grass. This model configuration can assist us in identifying the mechanisms responsible for the multiple peaks of the diurnal convection in Taiwan and can be applied to explain diurnal convection in other regions with similar environmental conditions. The existence of the plain area supports the presence of surface fluxes within the boundary layer and facilitates the development of sea breeze circulation, which enhances energy transport from both thermodynamic and dynamical aspects. To represent detailed turbulence evolution and convective structures, a high horizontal resolution (100-m) and output frequency (2-min) are used in this study, and the vertical grids are stretched with the resolution from 100 m to about 450 m at the model top (19 km), leading to a total number of 1024 × 1024 ×70 grids. Coriolis force is not considered in the simulations.

The 12-hr (06–18 LST) simulation with diurnally varying solar insolation is initialized with a conceptualized sounding representing a typical environment favoring local circulation development in summertime near Taiwan (Fig. 10a), according to the sounding observations from Ishigakijima in summertime weak synoptic condition from 2005 to 2014 (Fig. 11)[26]. The sounding is convectively unstable with no temperature inversion. The RH is greater than 80% below 800 hPa and is set to 54% at 500 hPa. The lifting condensation level (LCL), the level of free convection (LFC) and the tropopause are at about 0.4-km, 3.5-km and 10.5-km height, respectively. Due to the limited CAPE and the presence of convective inhibition (CIN) with a higher LFC, additional lifted mechanisms, such as upslope processes are required to overcome these inhibiting factors during the development of convection[54]. Therefore, this setup allows for the favorable development of local circulation, as it suppresses shallow convection in the plain area, preventing the occurrence of precipitation that could otherwise disrupt the local circulation. The sea surface temperature is uniformly prescribed as the lowest level air temperature of the initial condition (298.1 K) and is maintained constant throughout the time integration. As calm wind condition is given in all altitudes, the land-sea and mountain-valley breezes and convection triggering will be induced by horizontal buoyancy gradients in response to the surface heating differences of land-ocean temperature contrast and topography. We conducted 5 ensemble members for each experiment by adding temperature perturbations at the lowest model level.

To understand the diurnal convection under various environmental conditions, we carried out sensitivity experiments by decreasing RH at 500 hPa to 34% in the drier simulation and increasing to 74% in the wetter simulation. We named these simulations RH34, RH54, and RH74 simulations, respectively. The choice of these RH perturbations conforms to the

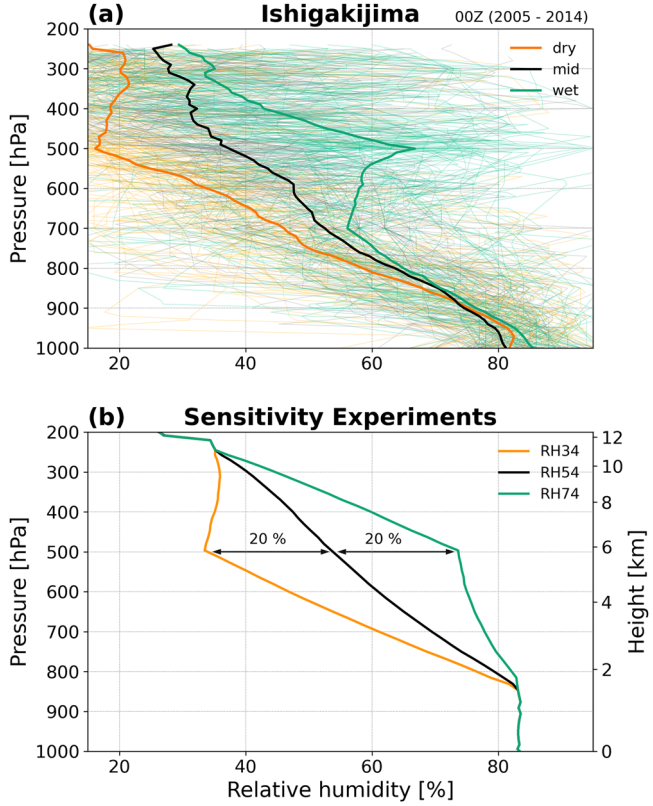


**Fig. 11 | Statistics of Ishigakijima sounding and initial conditions of sensitivity experiments. a** RH profiles from sounding observations at Ishigakijima during 2005 to 2014 under weak synoptic weather conditions. The black, orange, and green lines represent the 3 clusters of the driest 33%, middle 33%, and wettest 33% soundings according to the 500-hPa RH, respectively. The thicker lines represent the averaged profiles of the 3 clusters. **b** RH profiles for the initial conditions of the sensitivity experiments while changing the free troposphere moisture, with 500-hPa RH varied by 20% and uniform RH below about 1.5 km.

characteristics of the 3 clusters of the driest 33%, middle 33%, and wettest 33% sounding observations (Fig. 11). These profiles highlight the characteristics of observations and demonstrate the influence of subtropical high-pressure system strength on RH perturbations. The change of FTRH by 20% is critical to precipitation development and average intensity[24].

## Data availability

VVM simulation outputs used in this study are available upon request from the authors. CWA rain gauge observational data was downloaded from "Atmospheric Science Research and Application Databank (ASRAD)" supported by Chinese Culture University and the National Science and Technology Council, https://asrad.pccu.edu.tw/.

## Code availability

All codes for data analysis and visualization in this study are available at https://github.com/yuhsiuwang/IdealizedLES_diurnal_mount.git/.

Received: 2 July 2024; Accepted: 17 December 2024;
Published online: 26 December 2024

## References

1. Randall, D. A. & Tjemkes, S. Clouds, the Earth's radiation budget, and the hydrologic cycle. *Glob. Planet. Change* **4**, 3–9 (1991).
2. Birch, C. E., Parker, D., Marsham, J., Copsey, D. & Garcia-Carreras, L. A seamless assessment of the role of convection in the water cycle of the West African Monsoon. *J. Geophys. Res.: Atmos.* **119**, 2890–2912 (2014).
3. Mapes, B. E. & Houze, R. A. Jr Diabatic divergence profiles in western Pacific mesoscale convective systems. *J. Atmos. Sci.* **52**, 1807–1828 (1995).
4. Schumacher, C. & Houze, R. A. Jr Stratiform rain in the tropics as seen by the TRMM precipitation radar. *J. Clim.* **16**, 1739–1756 (2003).
5. Lintner, B. R., Holloway, C. E. & Neelin, J. D. Column water vapor statistics and their relationship to deep convection, vertical and horizontal circulation, and moisture structure at Nauru. *J. Clim.* **24**, 5454–5466 (2011).
6. Nesbitt, S. W. & Zipser, E. J. The diurnal cycle of rainfall and convective intensity according to three years of TRMM measurements. *J. Clim.* **16**, 1456–1475 (2003).
7. Krishna, U. M., Das, S. K., Deshpande, S. M. & Pandithurai, G. Physical processes controlling the diurnal cycle of convective storms in the Western Ghats. *Sci. Rep.* **11**, 14103 (2021).
8. Mori, S. et al. Diurnal land–sea rainfall peak migration over Sumatera Island, Indonesian Maritime Continent, observed by TRMM satellite and intensive rawinsonde soundings. *Monthly Weather Rev.* **132**, 2021–2039 (2004).
9. Ichikawa, H. & Yasunari, T. Time–space characteristics of diurnal rainfall over Borneo and surrounding oceans as observed by TRMM-PR. *J. Clim.* **19**, 1238–1260 (2006).
10. Yang, G. & Slingo, J. The Diurnal Cycle in the Tropics. *Monthly Weather Rev.* **129**, 784–801 (2001).
11. Dai, A. Global precipitation and thunderstorm frequencies. Part II: Diurnal variations. *J. Clim.* **14**, 1112–1128 (2001).
12. Dai, A. & Trenberth, K. E. The diurnal cycle and its depiction in the Community Climate System Model. *J. Clim.* **17**, 930–951 (2004).
13. Qian, J.-H. Why precipitation is mostly concentrated over islands in the Maritime Continent. *J. Atmos. Sci.* **65**, 1428–1441 (2008).
14. Wu, P., Yamanaka, M. D. & Matsumoto, J. The formation of nocturnal rainfall offshore from convection over western Kalimantan (Borneo) Island. *J. Meteorol. Soc. Jpn. Ser. II* **86**, 187–203 (2008).
15. Sato, T., Miura, H., Satoh, M., Takayabu, Y. N. & Wang, Y. Diurnal cycle of precipitation in the tropics simulated in a global cloud-resolving model. *J. Clim.* **22**, 4809–4826 (2009).
16. Su, C.-Y., Chen, W.-T. & Wu, C.-M. Object-based evaluation of tropical precipitation systems in DYAMOND simulations over the Maritime Continent. *J. Meteorol. Soc. Jpn. Ser. II* **100**, 647–659 (2022).
17. Birch, C. E. et al. Scale interactions between the MJO and the western Maritime Continent. *J. Clim.* **29**, 2471–2492 (2016).
18. Vincent, C. L. & Lane, T. P. A 10-Year austral summer climatology of observed and modeled intraseasonal, mesoscale, and diurnal variations over the Maritime Continent. *J. Clim.* **30**, 3807–3828 (2017).
19. Lu, J., Li, T. & Wang, L. Precipitation diurnal cycle over the Maritime Continent modulated by the climatological annual cycle. *J. Clim.* **34**, 1387–1402 (2021).
20. Wei, Y., Pu, Z. & Zhang, C. Diurnal cycle of precipitation over the Maritime Continent under modulation of MJO: Perspectives from cloud-permitting scale simulations. *J. Geophys. Res. -Atmos.* **125**, e2020JD032529 (2020).
21. Peatman, S. C. et al. The role of density currents and gravity waves in the offshore propagation of convection over Sumatra. *Mon. Weather Rev.* **151**, 1757–1777 (2023).
22. Tian, Y., Zhang, Y. & Klein, S. A. What determines the number and the timing of pulses in afternoon precipitation in the Green Ocean Amazon (GoAmazon) observations? *Geophys. Res. Lett.* **49**, e2021GL096075 (2022).
23. Zhuang, Y., Fu, R., Marengo, J. A. & Wang, H. Seasonal variation of shallow-to-deep convection transition and its link to the environmental conditions over the Central Amazon. *J. Geophys. Res.: Atmos.* **122**, 2649–2666 (2017).
24. Wu, C.-M., & Chen, P.-Y. Idealized cloud-resolving simulations of land-atmosphere coupling over tropical islands. *Terrest. Atmos. Oceanic Sci.* **32** (2021).

25. Kuo, Y.-H., Neelin, J. D. & Mechoso, C. R. Tropical convective transition statistics and causality in the water vapor–precipitation relation. *J. Atmos. Sci.* **74**, 915–931 (2017).
26. Chang, Y.-H., Chen, W.-T., Wu, C.-M., Moseley, C. & Wu, C.-C. Tracking the influence of cloud condensation nuclei on summer diurnal precipitating systems over complex topography in Taiwan. *Atmos. Chem. Phys.* **21**, 16709–16725 (2021).
27. Kuo, K.-T. & Wu, C.-M. The precipitation hotspots of afternoon thunderstorms over the Taipei Basin: Idealized numerical simulations. *J. Meteorol. Soc. Jpn. Ser. II* **97**, 501–517 (2019).
28. Chang, Y. H., Chen, W. T., Wu, C. M., Kuo, Y. H. & Neelin, J. D. Identifying the Deep-Inflow Mixing Features in Orographically-Locked Diurnal Convection. *Geophys. Res. Lett.* **50**, e2023GL103107 (2023).
29. Chen, W. T., Chang, Y. H., Wu, C. M. & Huang, H. Y. The future extreme precipitation systems of orographically locked diurnal convection: the benefits of using large-eddy simulation ensembles. *Environ. Res.: Clim*. (2024).
30. Kirshbaum, D. J. & Smith, R. B. Orographic precipitation in the tropics: Large-eddy simulations and theory. *J. Atmos. Sci.* **66**, 2559–2578 (2009).
31. Ahmed, F. & Neelin, J. D. Reverse Engineering the Tropical Precipitation–Buoyancy Relationship. *J. Atmos. Sci.* **75**, 1587–1608 (2018).
32. Schiro, K. A., Ahmed, F., Giangrande, S. E. & Neelin, J. D. GoAmazon2014/5 campaign points to deep-inflow approach to deep convection across scales. *Proc. Natl Acad. Sci.* **115**, 4577–4582 (2018).
33. Ahmed, F., Adames, Á. F. & Neelin, J. D. Deep Convective Adjustment of Temperature and Moisture. *J. Atmos. Sci.* **77**, 2163–2186 (2020).
34. De Rooy, W. C. et al. Entrainment and detrainment in cumulus convection: an overview. *Q. J. R. Meteorol. Soc.* **139**, 1–19 (2013).
35. Dai, Y., & Williams, I. N. Land surface effects on shear balance of squall lines. *J. Geophys. Res.: Atmos.* **127** (2022).
36. Rotunno, R., Klemp, J. B. & Weisman, M. L. A theory for strong, long-lived squall lines. *J. Atmos. Sci.* **45**, 463–485 (1988).
37. Wu, C.-M., Lin, H.-C., Cheng, F.-Y. & Chien, M.-H. Implementation of the land surface processes into a vector vorticity equation model (VVM) to study its impact on afternoon thunderstorms over complex topography in Taiwan. *Asia-Pac. J. Atmos. Sci.* **55**, 701–717 (2019).
38. Hsieh, M.-K., Chen, Y.-W., Chen, Y.-C. & Wu, C.-M. The Roles of Local Circulation and Boundary Layer Development in Tracer Transport over Complex Topography in Central Taiwan. *J. Meteorol. Soc. Jpn. Ser. II* **100**, 555–573 (2022).
39. Hsu, T.-H., Chen, W.-T., Wu, C.-M. & Hsieh, M.-K. The observation-based index to investigate the role of the lee vortex in enhancing air pollution over northwestern Taiwan. *J. Appl. Meteorol. Climatol.* **62**, 427–439 (2023).
40. Hwang, W.-C., Lin, P.-H. & Yu, H. The development of the "Storm Tracker" and its applications for atmospheric high-resolution upper-air observations. *Atmos. Meas. Tech.* **13**, 5395–5406 (2020).
41. Jung, J.-H. & Arakawa, A. A three-dimensional anelastic model based on the vorticity equation. *Monthly Weather Rev.* **136**, 276–294 (2008).
42. Wu, C. M., & Arakawa, A. Inclusion of surface topography into the vector vorticity equation model (VVM). *J. Adv. Modeling Earth Syst.* **3**. (2011).
43. Chien, M.-H. & Wu, C.-M. Representation of topography by partial steps using the immersed boundary method in a vector vorticity equation model (VVM). *J. Adv. Model. Earth Syst.* **8**, 212–223 (2016).
44. Shutts, G. J. & Gray, M. E. B. A numerical modelling study of the geostrophic adjustment process following deep convection. *Q. J. R. Meteorol. Soc.* **120**, 1145–1178 (1994).
45. Chen, F. et al. Modeling of land surface evaporation by four schemes and comparison with FIFE observations. *J. Geophys. Res.: Atmos.* **101**, 7251–7268 (1996).
46. Chen, F. & Dudhia, J. Coupling an advanced land surface–hydrology model with the Penn State–NCAR MM5 modeling system. Part I: Model implementation and sensitivity. *Monthly Weather Rev.* **129**, 569–585 (2001).
47. Morrison, H. & Milbrandt, J. A. Parameterization of cloud microphysics based on the prediction of bulk ice particle properties. Part I: Scheme description and idealized tests. *J. Atmos. Sci.* **72**, 287–311 (2015).
48. Huang, J. D. & Wu, C. M. Effects of microphysical processes on the precipitation Spectrum in a strongly forced environment. *Earth Space Sci.* **7**, e2020EA001190 (2020).
49. Tsai, W. M. & Wu, C. M. The environment of aggregated deep convection. *J. Adv. Model. Earth Syst.* **9**, 2061–2078 (2017).
50. Chen, W.-T., Wu, C.-M., Tsai, W.-M., Chen, P.-J. & Chen, P.-Y. Role of coastal convection to moisture buildup during the South China Sea summer monsoon onset. *J. Meteorol. Soc. Jpn. Ser. II* **97**, 1155–1171 (2019).
51. Chen, Y. T. & Wu, C. M. The role of interactive SST in the cloud-resolving simulations of aggregated convection. *J. Adv. Model. Earth Syst.* **11**, 3321–3340 (2019).
52. Huang, J. D., Hung, C.-S., Wu, C. M. & Miura, H. Convective Variabilities Leading to Different Pathways of Convective Self-aggregation in Two Cloud-resolving Models. *J. Atmos. Sci.* **80**, 2041–2055 (2022).
53. Huang, J. D. & Wu, C. M. A Framework to Evaluate Convective Aggregation: Examples With Different Microphysics Schemes. *J. Geophys. Res.: Atmos.* **127**, e2021JD035886 (2023).
54. Wu, P. Y. & Takemi, T. Impacts of mountain topography and background flow conditions on the predictability of thermally induced thunderstorms and the associated error growth. *J. Atmos. Sci.* **80**, 1177–1199 (2023).


## Acknowledgements

This work was supported by the National Science and Technology Council of Taiwan through Grants NSTC112-2123-M-002-006, NSTC112-2111-M-002-008, NSTC112-2111-M-002-015, NSTC113-2111-M-002-013, and National Taiwan University Grants NTU-114L7819 and NTU-113L7841. The authors sincerely thank the National Center for High-performance Computing (NCHC) and Central Weather Administration (CWA) for providing the high-performance computation platform to conduct the simulations.

## Author contributions

Y.H.W., W.T.C. and C.M.W. designed the experiments, and C.M.W. performed the simulations. Y.H.W. developed the code for analyzing and displaying model results. Y.H.W. and W.T.C. prepared the manuscript with contributions from all co-authors. All authors reviewed and approved the manuscript.

## Competing interests

The authors declare no competing interests.

## Additional information

**Supplementary information** The online version contains supplementary material available at https://doi.org/10.1038/s41612-024-00884-y.

**Correspondence** and requests for materials should be addressed to Wei-Ting Chen.